Multifunctional Applications Enabled by Fluorination of Hexagonal Boron Nitride

Devashish Salpekar[§], Peter Serles[§], Guillaume Colas, Li Ma, Shwetank Yadav, Mahdi Hamidinejad, Valery N Khabashesku, Guanhui Gao, Venkataraman Swaminathan, Robert Vajtai, Chandra Veer Singh, Chul Park, Tobin Filleter, AshokKumar Meiyazhagan*, Pulickel M. Ajayan**

D. Salpekar, V. N. Khabashesku, G. Gao, V. Swaminathan, R. Vajtai, A. Meiyazhagan, P. M. Ajayan
Department of Materials Science & NanoEngineering, 6100 Main Street, Rice University, Houston, TX 77005, U.S.A.
E-mail: ajayan@rice.edu (P. M. Ajayan), ma37@rice.edu (A. Meiyazhagan)

P. Serles, L. Ma, C. Park, T. Filleter
Department of Mechanical & Industrial Engineering, The University of Toronto, 5 King's College Road, Toronto, ON, Canada, M5S 3G8
Email: filleter@mie.utoronto.ca (T. Filleter)

G. Colas
Université de Franche-Comté, CNRS, institut FEMTO-ST, F-25000 Besançon, France

S. Yadav, C. V. Singh
Department of Materials Science and Engineering, University of Toronto; 184 College St, Toronto, ON, Canada, M5S 3E4

M. Hamidinejad
Department of Engineering, University of Cambridge, Cambridge, United Kingdom, CB30FS
Department of Mechanical Engineering, University of Alberta, 9211-116 Street NW, Edmonton, AB T6G1H9, Canada

[§] D. Salpekar and P. Serles contributed equally

Keywords: Functionalization, 2D Materials, Lubricant, Nanofillers, Dielectrics, Hexagonal Boron Nitride

Two-dimensional (2D) materials exhibit exceptional properties as compared to their macroscopic counterparts, with promising applications in nearly every area of science and technology. To unlock further functionality, the chemical functionalization of 2D structures is a powerful technique that enables tunability and new properties within these materials. Here, we exploit the successful effort to chemically functionalize hexagonal Boron Nitride (*h*BN), a chemically inert 2D ceramic with weak interlayer forces, using a gas-phase fluorination process. The fluorine functionalization guides interlayer expansion and increased polar surface charges on the *h*BN sheets resulting in a number of vastly improved applications. Specifically, the F-*h*BN exhibits enhanced dispersibility and thermal conductivity at higher temperatures by more than 75% offering exceptional performance as a thermofluid additive. Dispersion of low volumes of F-*h*BN in lubricating oils also offers marked improvements in lubrication and wear resistance for steel tribological contacts decreasing friction by 31% and wear by 71%. Additionally, incorporating numerous negatively charged fluorine atoms on *h*BN induces a permanent dipole moment, demonstrating its applicability in microelectronic device applications. Our findings suggest that anchoring chemical functionalities to *h*BN moieties improves a variety of properties for *h*-BN, making it suitable for numerous other applications such as fillers or reinforcement agents and developing high-performance composites structures.

1. Introduction

Hexagonal boron nitride (*h*BN), a two-dimensional analog of graphene, has an alternating arrangement of boron and nitrogen atoms in a honeycomb lattice structure. Within the *h*BN layer, the boron and nitrogen atoms are linked together through strong sp^2 covalent bonds, while the adjacent layers are held via weaker van der Waals forces. As such, *h*BN presents a unique structural characteristic among the family of 2D materials as each boron atom lies above and below a nitrogen atom in the (001) plane. This enables *h*BN to present partial charge distribution, no charge delocalization, no in-plane or out-of-plane electron conduction and therefore exhibits a high bandgap[1] and exceptional dielectric properties.[2] Additionally, owing to its van der Waals structure akin to graphite, *h*BN offers exceptional lubricating properties[3,4] and bulk *h*BN possesses one of the highest thermal conductivities among high bandgap materials approaching 400 W/mK at room temperature and making it comparable to copper and silver.[2] As such, *h*BN has been widely explored as a nano additive in lubricant and coolant fluids[5–7] and a dielectric material in 2D field-effect transistors.[8] All these applications are further enabled by *h*BN's excellent chemical and thermal stability,[9] which qualifies it for implementation in a wide range of environments and a wide diversity of promising applications.

While *h*BN is considered a promising lubricating, thermal management, and dielectric material, wide-scale implementation of *h*BN for these multifunctional applications is hindered by several inherent limitations. For example, *h*BN, like other nanoparticles such as graphene, MoS_2, WS_2 etc., exhibits poor dispersion and aggregation at higher loadings.[10–12] The dispersed nanoparticles must synergize with the fluid to maintain high-level dispersion, stability, and adhesion when distributed which is largely solvent dependent.[13,14] Additionally, *h*BN demonstrates enhanced thermal conductivity as the number of layers decreases, owing to reduced interlayer coupling and fewer phonon branches and states available for Umklapp scattering,[15,16] so must be employed in nanoscale morphologies for high effectiveness. Meanwhile, for effective lubricating performance, *h*BN requires higher layer numbers but reduced particle sizes thereby requiring controlled processing.[17,18] To address these challenges, chemical functionalization has emerged as a practical approach to achieve effective dispersion, exfoliation, and further enhancement of inherent properties for macroscopic applications.[19–21] The unique structure of *h*BN results in partial ionicity whereby partial positive charge occurs in electron-deficient B atom centers and partial negative charge in electron-rich N atom centers. This characteristic makes the B sites susceptible to nucleophilic groups while the N sites demonstrate reactivity towards electrophilic species.[22] Extensive exploration has been conducted on diverse chemical functionalization routes, such as hydroxyl (-OH),[11,23] alkyl (-R),[24] amino ($-NH_2$),[25,26] heteroatoms (C and O),[27] and surfactants.[28] Further discussions of functional group anchoring and functionalization strategies have been covered in the works of Weng[29] and Li[30]. Nonetheless, investigation of fluorinated *h*BN chemistries remains relatively limited. Previous attempts to fluorinate *h*BN have relied on harsh chemicals like ammonium fluoride[31] and Nafion[32] combined with hydrothermal treatments, ball-milling, and extensive processing. These approaches often sacrifice *h*BN's intrinsic properties, resulting in defect-rich *h*BN with excessive processing times.

Here, we employ a facile gas-phase fluorination technique to covalently functionalize *h*BN with fluorine moieties.[21] This technique is straightforward, batch scalable, and does not require additional chemicals or post-treatment processing, thereby preserving and enhancing the unique qualities of *h*BN without the introduction of defects. Analytical and computational evaluation highlights the structural changes upon fluorination of *h*BN whereby fluorine atoms expand the interlayer distance, improving exfoliation and decreasing interlayer coupling, thereby enhancing lubrication and thermal dissipation characteristics. Additionally, the polarity generated in the F-*h*BN surfaces due to fluorine atoms can aid in the effective dispersion of F-*h*BN in lubricants, and the electronegative fluorine expands the dielectric polarization of *h*BN facilitating dielectric tunability with fluorine concentration. Collectively, these multifaceted applications which are enabled by the fluorination of *h*BN offer exceptional applicability for high thermal dissipation fluids, high-temperature lubrication, microelectronic insulation, and many other applications.

2. Results

2.1. Fluorination of *h*BN

Batch-scale fluorination of 70 nm *h*BN particles was performed at two different conditions of 50ºC and 90ºC for 2 hours, as described in the Methods section. X-Ray Photoelectron Spectroscopy (XPS) confirms the 50ºC with 2h fluorination displayed 9.4 atomic percentage (at.%) fluorine, while fluorination at 90ºC with 2h exhibited 5.2 at.% fluorine (**Figure S1**). The increased fluorination at lower temperature is due to the volatility of the weak ionic N-F bond which decomposes beyond 60ºC.[21] **Figure 1A&B** display scanning transmission electron microscopy (STEM) images of the synthesized F-*h*BN samples with 9.4 at.% fluorine. Figure 1A and **S2** demonstrates the easy exfoliation of F-*h*BN due to the lamellar structure resulting in few-layer thick F-*h*BN sheets. As demonstrated in **Figure 1B**, the F-*h*BN retains its crystalline structure indicating the fluorination process did not trigger any crystallographic damage such as defects or impurities in the derived F-*h*BN structures despite achieving complete fluorine coverage as seen in the energy dispersive spectroscopy (EDS) mapping in **Figure 1C**. Preserving this crystallinity of *h*BN is an essential criterion for several applications including the dielectric[33] and thermal performance of *h*BN.[34] This is in contrast with the majority of chemical treatments which cause densification and defect formation of *h*BN nanoparticles due to the aggressive chemical treatments required for the chemical functionalization and extensive washing procedures of functionalized *h*BN.[35] It should also be noted that 70 nm *h*BN nanoparticles achieved higher degrees of fluorination by as much as 1.8 at.% as compared to 800 nm nanoparticles under equivalent processing conditions due to the increased surface area.

The structural characteristics of the F-*h*BN are further investigated by X-Ray Diffraction (XRD) with the diffraction peaks displayed in **Figure 1D**. The pristine *h*BN powders display a peak at 26.92º, corresponding to the (002) plane in *h*BN.[10] Meanwhile, the 9.4 at.% F-*h*BN shows a similar (002) plane with a downshift to 26.54º suggesting an increased interlayer distance due to the intercalation of fluorine while still retaining the inherent crystal structure of *h*BN.[36,37] Raman spectroscopy is further used to identify structural alterations upon fluorination for the pristine, 5.2 at.%, and 9.4 at.% F-*h*BN powders, and the results are presented in **Figure 1E**. The pure *h*BN displays a Raman shift at 1365.85 cm^{-1}, corresponding to the E_{2g} in-plane phonon mode of *h*BN. In contrast, the fluorinated *h*BN exhibited a redshift attributed to the expansion of *h*BN layers by intercalation, as is frequently observed in doped or functionalized 2D materials.[38] The 5.2 at.% F-*h*BN exhibits a redshift by 0.17 cm^{-1} (E_{2g} at 1365.77 cm^{-1}), and the redshift continues with higher fluorine content as 9.4 at.% presents the E_{2g} peak at 1365.57 cm^{-1}. Both XRD and Raman indicate interlayer expansion by sp^3 bonded intercalated fluorine, akin to graphene oxide, which is calculated to be energetically favorable as per prior DFT studies of F-*h*BN.[32,39] We further confirm this interlayer expansion by atomic force microscope monolayer thickness measurements which demonstrate $c_{F\text{-}hBN}$=4.36 ± 0.2Å and c_{hBN}= 3.23 ± 0.1Å (**Figure S3**). We also note the intensity of the Raman peak in *h*BN increases in proportion

to the square of the induced dipole moment. Adding fluorine strengthens the dipole moment of the B-N bond, resulting in higher peak intensities, as demonstrated in Figure 1E.

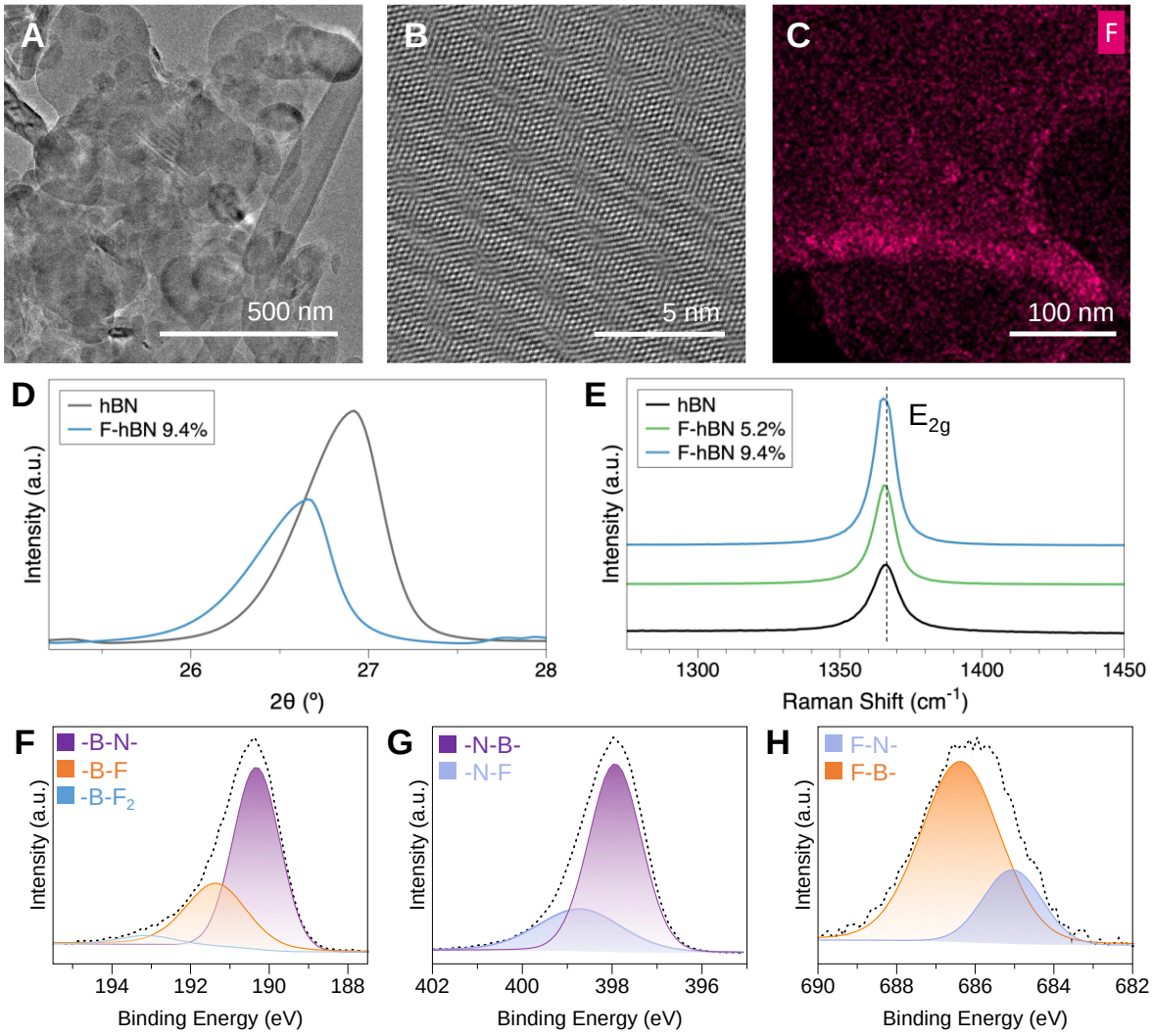

Figure 1. Fluorination of *h*BN. (A) Lower magnification STEM images of *h*BN following fluorination process showing crystallinity and several stacked exfoliated sheets. (B) High-resolution STEM image of the F-*h*BN sheets displaying an absence of crystallographic damage such as defects or impurities. (C) EDX mapping of F-Kα signal for a single particle showing complete fluorine coverage in the F-*h*BN sample. (D) The XRD of the *h*BN and F-*h*BN peak (002) displayed a downshift upon fluorination, indicative of increased c-spacing. (E) Raman spectroscopy showing a redshift with increasing fluorine content, and (F-H) Displays deconvoluted high-resolution XPS spectra of F-*h*BN- 50ºC/2h sample with 9.4 at.% fluorine coverage and their corresponding B*1s*, N*1s*, and F*1s* spectra.

XPS is employed to reveal the specific bonding states of fluorine within the *h*BN structure with the B*1s*, N*1s*, and F*1s* spectra for 9.4 at.% F-*h*BN shown in **Figure 1F-H**, respectively. XPS spectra of the 5.2 at.% F-*h*BN are included in **Figure S4**. The deconvoluted B*1s* spectra (Figure 1F and S4A) of both the samples exhibit a dominant peak at 190.3 eV due to the presence of -B-N- bonds in the *h*BN, and two additional peaks are noted around 191 and 193 eV, which correspond to the presence of -B-F and -B-F_2 groups, respectively. It is important to note that

the -B-F bonds can form on both edges and in-plane, while -B-F_2 bond formation is favorable only at edge sites of the *h*BN sheets, which agrees with the relative signal intensity.[3,31,40] Similarly, the deconvoluted N*1s* spectra (Figure 1G and S4B) display two distinct bands, the first at 398 eV, corresponding to -N-B- bonding in *h*BN, and the second band at 398.7 eV assigned to the fluorine bonded to nitrogen (N-F) atoms. Interestingly, the N-F bond has a downward shift in the binding energy due to the high electronegativity of nitrogen and fluorine atoms.

The F1s spectra are deconvoluted into two major bands seen around 686.6 and 685.4 eV, as shown in Figures 1H and S4C**.** The first peak at 686 eV represents the fluorine bonded with boron, resulting in covalently connected -B-F signals. The other peak around 685 eV was the weaker signals arising due to -N-F peaks. Importantly, no noticeable traces of free fluorine (F_2) signals were seen in any fluorinated samples, suggesting adequate fluorine bonding with the BN sites. By relative peak intensity in the F*1s* spectra, we identify a ratio of 78% to 22% for -B-F bonding compared to -N-F bonding indicating a clear preferential binding site for fluorine. This ratio is consistent for both the 9.4 at.% F-*h*BN and 5.2 at.% F-*h*BN samples indicating an inherent preferential bonding.[21,39] This observation was further confirmed through Fourier-Transform Infrared (FTIR) analysis (**Figure S5**), where the F-*h*BN displayed two additional signals with the minor signal around 520 cm^{-1} corresponding to asymmetric N-F bending vibrations and a pronounced peak at ~1030 cm^{-1} due to B-F bonds. The presence of fluorine in the samples was further confirmed using electron energy loss spectroscopy (EELS), STEM high-angle annular dark-field imaging (HAADF), and Energy Dispersive X-ray (EDX) analysis with their results presented in **Figures S6-S9,** respectively.

It should be noted that while fluorinated compounds have been identified to present health and environmental hazards, the present exploit of F-hBN requires <0.1 wt.% concentrations of nanoparticles, which themselves have <10 at.% fluorine concentrations, to achieve significant enhancements for several engineering applications. The handling, deployment, and disposal procedures for 70 nm nanoparticles already include health and environmental considerations which mitigate the risks posed by the minor addition of fluorine.

2.2. F-*h*BN Dispersion in Nanofluids

*h*BN is inherently an exceptional thermal conductor; hence, we investigated the effect of the thermal conductivity of *h*BN and F-*h*BN sheets by dispersion them in mineral oil to create a thermally conductive nanofluid. The base mineral oil exhibits a thermal conductivity of ~0.116 W/mK at 298K with no variation in temperature. Various combinations of pristine *h*BN and 9.4 at.% F-*h*BN dispersed nanofluids with 0.001, 0.005, and 0.1 wt.% loading in mineral oil were prepared (**Figure S10**) and the measured thermal properties of all the dispersions are listed in **Table S1** and **S2**. The addition of pristine *h*BN exhibits an increase in thermal conductivity of 2.59%, 5.17%, and 7.76% for three different loading concentrations, respectively, as shown in **Figure 2A**, which matches the lower boundary values reported before.[41] Meanwhile, the

fluorinated *h*BN dispersed mineral oil with the same three concentrations exhibited a significant increase in the thermal conductivity of ~9.44%, 11%, and 12%. This enhanced thermal conductivity is nearly double that provided by equivalent loading percentages of hBN[42] or graphene[43] in mineral oils. Moreover, even at these lower concentrations, F-*h*BN shows a remarkable increase compared to *h*BN in mineral oil. This substantial increase in thermal conductivity, especially at lower concentrations, is due to two primary reasons: i) increased interlayer spacing resulting in effective exfoliation of F-*h*BN sheets which considerably improves the dispersion of F-*h*BN layers in mineral oil and ii) increased surface charge on *h*BN due to fluorination.[44]

To further understand the mechanism of thermal conductivity enhancement due to fluorination, we evaluate F-*h*BN nanofluids derived with two different fluorine concentrations up to the maximum loading of 9.4 at.% F-*h*BN while maintaining the nanofiller loading at 0.01 wt% **(Figure 2B**). At 298K, 9.4 at.% F-*h*BN dispersed mineral oil displayed a greater thermal conductivity enhancement than mineral oil with 5.2 at.% F-*h*BN. This supports our assumption on fluorine's role in improving the dispersion of F-*h*BN in mineral oil, which can also be attributed to highly polar surface charges resulting in increased interaction between fluorine's lone pair electrons and the aliphatic chains in mineral oil. Importantly, the relative enhancement in conductivity is substantial at higher temperatures; at 323K and 348K, the 5.2 at.% F-*h*BN dispersed lubricant shows a 41% and 45% increase in thermal conductivity while the 9.4 at.% F-*h*BN exhibits a marked increase of 69% and 76%, respectively.

We also considered the thermal conductivity enhancement with respect to nanofiller concentration up to 0.1 wt.% at 298K and 323K (**Figure 2C**). At room temperature, the thermal conductivity of 9.4 at.% F-*h*BN dispersed mineral oil exhibits a trend where the enhancement increases gradually from 10.2% for 0.001 wt.% to 41% for the 0.1 wt.% concentration. On increasing the temperature to 323K, an unusual trend is observed where the enhancement in thermal conductivity nicely increases from 21% at 0.001 wt.% to 69% at 0.01 wt.% loading. This notable increase is attributed to enhanced dispersion observed with more fluorine concentrations, improved Brownian motion, and phonon-electron interaction at elevated temperature.[45]

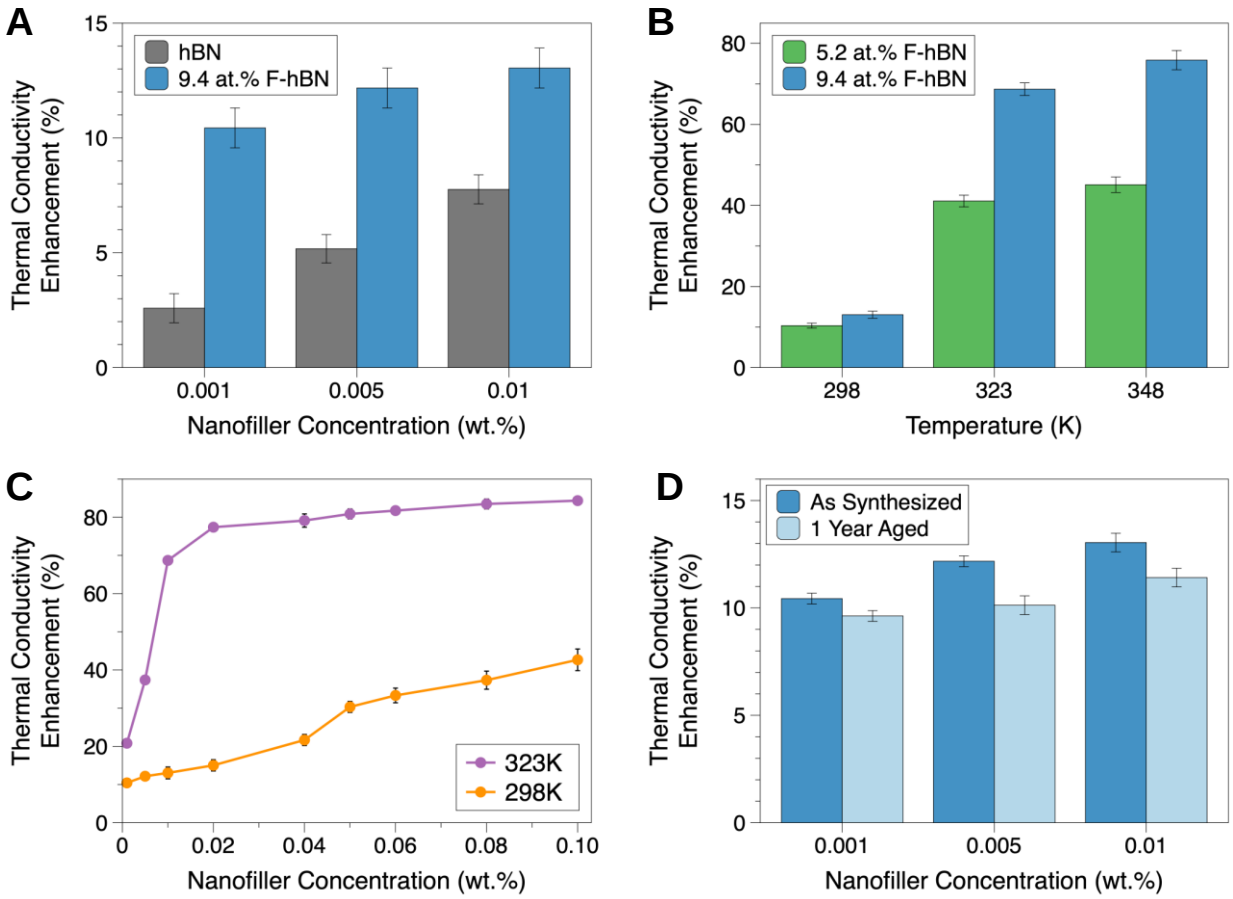

Figure 2. Thermal conductivity enhancement of F-*h*BN nanoparticles dispersed in mineral oil. (A) Thermal conductivity enhancement comparison of nanofluids containing pristine *h*BN and 9.4 at.% F-*h*BN displayed an increase in thermal conductivity at three different concentrations. (B) Effect of change in fluorine content versus temperature and their corresponding thermal conductivity measurements. The thermal conductivity of both the F-*h*BN dispersed nanofluids increases with temperature increase which is attributed to highly polar surface charges resulting in increased interaction between fluorine's lone pair electrons and the aliphatic chains in mineral oil. (C) Thermal conductivity correlation with the concentration of 9.4 at.% F-*h*BN in mineral oil at two different temperatures of 298K and 323K, which is due to enhanced dispersion observed with more fluorine concentrations and excitation of phonon modes and Brownian motion at elevated temperatures. (D) 'Shelf life' of nano-fluids, prepared using 9.4 at.% F-*h*BN with measured thermal conductivity of as-synthesized and the same dispersion after one year displaying a minimal decrease in thermal conductivity. All samples were tested with N>5 and error bars represent standard error.

Finally, we evaluate the practical implementation of the derived F-*h*BN dispersed mineral oil, including its longevity and changes in the thermal conductivity over a prolonged period. Mineral oil samples with the three different concentrations of 9.4 at.% F-*h*BN were evaluated as-synthesized and subsequently left undisturbed for 12 months. As the nanofillers naturally settled throughout this period, the F-*h*BN mineral oil dispersions were uniformly stirred at 500rpm for 1 hour before thermal conductivity measurements. The thermal conductivity of the aged nanofluid exhibits only a minor decrease after one year, demonstrating the effectiveness of F-*h*BN over prolonged durations for practical conditions (**Figure 2D**). Even after a one-year

duration, the thermal conductivity of the F-*h*BN is significantly higher than the pristine *h*BN, demonstrating the stability of fluorination for thermal conductivity enhancement. Overall, despite *h*BN already exhibiting outstanding capabilities for developing high thermally conducting fluids, we present a further enhancement of these exceptional properties by fluorination which resulted in enhanced dispersion and stability without degrading the inherent unique characteristics of *h*BN. Specifically, the remarkable enhancement in thermal conductivity at low concentrations (<0.1 wt.%) by as much as a factor of two compared to pristine *h*BN suggests a facile and inexpensive approach to obtaining nanofluids with superior thermal conductivity performances.

In addition to its use as a filler in mineral oil, we studied how F-*h*BN disperses and remains stable in various solvents. More information and discussion is available in **Figures S11-S13**. When F-*h*BN is dispersed in mineral oil, it exhibits different dispersion properties than mixed in organic solvents. Mineral oil contains higher alkanes with nine or more carbon atoms and is more viscous than most organic solvents. Adding F-*h*BN to mineral oil improves intermolecular and surface interactions thereby increasing the lubricant's dispersion and stability. Also, factors such as solvent molecular size and density, and *h*BN particle size, morphology, and fluorination coverage can affect the interaction between alkanes and fluorinated *h*BN. We dispersed F-*h*BN in different solvents and examined the dispersions visually (**Figure S11**), using UV-Vis (**Figure S12),** and Zeta potential measurements (**Figure S13**). We identify that polar solvents such as Isopropyl alcohol (IPA) and dimethyl sulfoxide (DMSO) exhibited excellent dispersion stability reaching concentrations as high as 0.2 mg/mL without notable agglomeration while weakly polar dichloromethane (DCM) and water experience aggregation at lower concentrations. A detailed discussion on dispersion, stability and outcomes are included in the supporting information.

2.3. F-*h*BN as Lubricating Nanoparticles

The van der Waals bonding between layers of *h*BN creates a natural solid lubricating material akin to graphene, which is commonly employed as a nanoparticle additive in lubricating oils to decrease the coefficient of friction (CoF, μ) and the wear rates of interfacing tribological contacts. Nanoparticles suspended in lubricating oils become trapped between the sliding faces and compacted onto the surface into a lubricating tribofilm.[46,47] This tribofilm evens the surface's roughness and, for 2D materials such as *h*BN, the tribofilm typically consists of oriented van der Waals layers that shear to provide low friction at the interface.[48,49] It has been previously demonstrated that adding *h*BN nanoparticles in lubricating oils can significantly decrease the coefficient of friction by up to 20%, with optimal loading ranges of <0.5 wt.% *h*BN.[4,18,50] Additionally, tribological studies of *h*BN additives in oil lubricants have shown significant dependence on the size of the additive particles, where ultrafine 70 nm *h*BN particles have exhibited a third of the coefficient of friction of 5 μm *h*BN particle additives.[18]

In our experiments, we consider three different loading concentrations of nanoparticles dispersed in mineral oil (0.01, 0.05, and 0.1 wt.%) as compared to conventional mineral oil. We

use the highest fluorine loading of 9.4 at.% F-hBN for all three concentrations in comparison to pristine hBN. The contact of a linear reciprocating tribometer was then submerged in each of the lubricating oils and run for 8,500 cycles, corresponding to 102m of travel, at 1 GPa contact pressure between AISI 52100 steel contacts. The results of the average per-cycle coefficient of friction of the base mineral oil and the optimal concentrations of *h*BN and F-*h*BN for 8500 cycles are presented in **Figure 3 A-C.** The average friction for all 7 tested configurations can be seen in **Supplementary Figure S14**. Compared to the control mineral oil (Figure 3A), the addition of pristine *h*BN (Figure 3B**)** exhibits a decrease in the average CoF by 17% for the 0.1 wt%. loading, which agrees with previous works on *h*BN nanoparticle lubricants.[4,18,50] Furthermore, it is seen that the cycle-to-cycle standard deviation decreases by 55%, suggesting increased stability of the contact conditions.

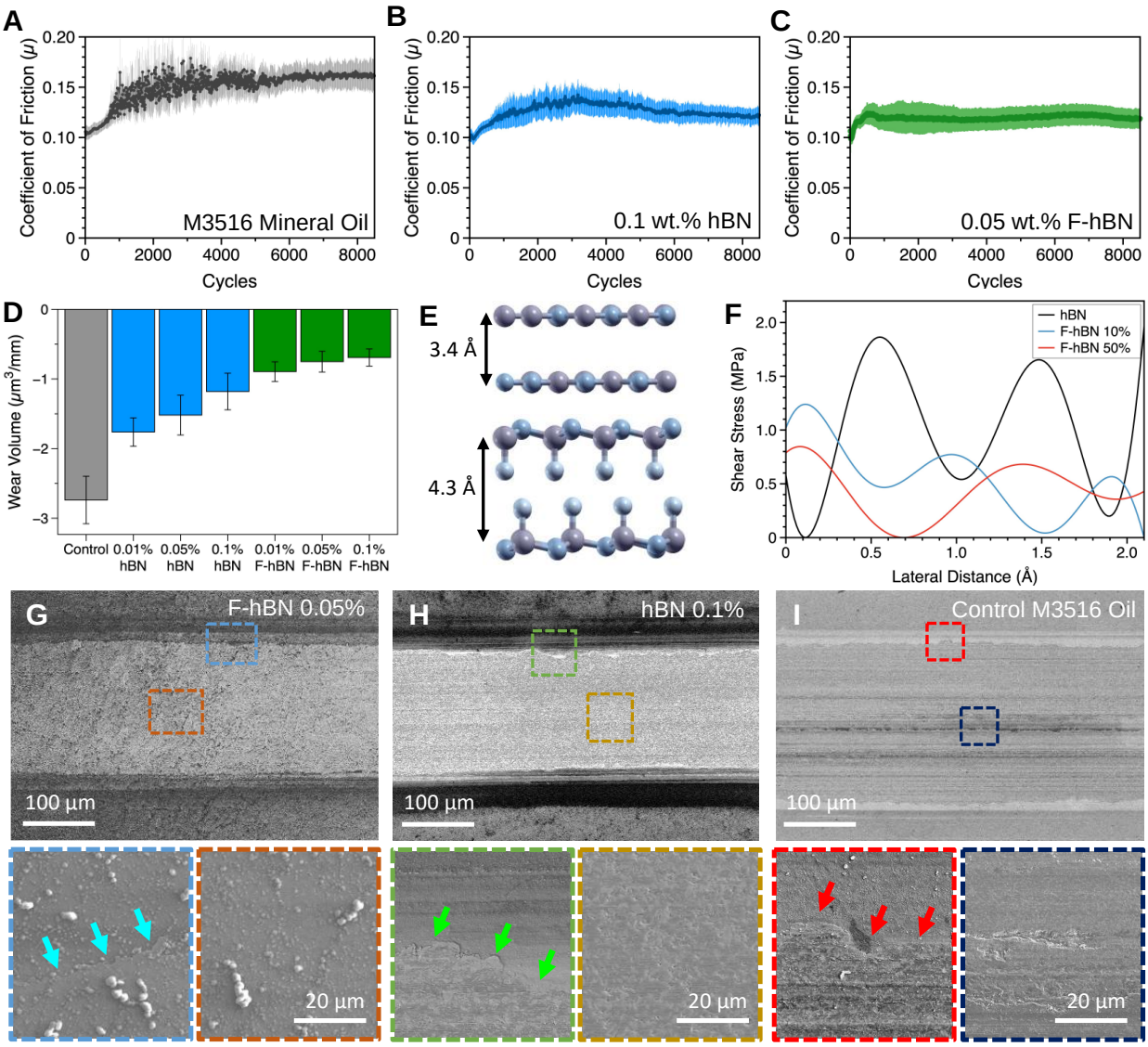

Figure 3. Friction and wear behavior of pristine and fluorinated *h*BN nanoparticle additives dispersed in M3516 mineral oil. (A-C) Averaged friction coefficients from 3 runs of 8500 cycles for plain mineral oil, 0.1% hBN additive, and 0.05% F-*h*BN additive, respectively. (D) Average wear volumes of the friction track per mm traveled for the 7 different configurations. (E) Density functional theory schematics of pristine *h*BN sheets and F-*h*BN with 50% F coverage, respectively, where the F-*h*BN

displays an increased interlayer spacing from 3.4 Å to 4.3 Å due to intercalation. (F) Shear stress of sliding between sheets for 0%, 10%, and 50% fluorine coverage of *h*BN. (G-I) Scanning electron microscope images of the wear track for 0.05 wt.% F-*h*BN additives, 0.1 wt.% *h*BN additives, and the control mineral oil. Arrows in the subset images indicate the tribofilm edge contrasted against the steel substrate. A-C are averaged values of N=3 with highlighted region representing standard deviation per cycle. Wear volumes in D are each averaged from N=3 with error bars representing standard error.

Upon fluorination of the nanoparticle additives, the F-*h*BN dispersed lubricants demonstrate a further 12% decrease in the CoF for 0.05 wt.% as compared to using plain *h*BN additives. This CoF for F-*h*BN of $\mu=0.117 \pm 0.01$ is also considerably lower than prior explorations of hBN for dispersed nanoparticle lubricated steel contacts.[18] Additionally, the cycle-to-cycle standard deviation decreases by a further 84% for the oil prepared with 0.05 wt% of F-*h*BN, demonstrating very stable contact conditions that are crucial for low-noise machinery. Interestingly, we observed the lowest CoF for 0.05 wt.% F-*h*BN as $\mu=0.117 \pm 0.001$ while the higher loading of 0.1 wt.% F-*h*BN showed an increase in CoF of $\mu=0.123 \pm 0.003$. This suggests that the optimal tribological loading conditions of F-*h*BN occur at a lower loading percentage than pristine *h*BN, which highlights the inexpensive additive requirement.

The decrease in CoF with the addition of 0.05 wt.% F-*h*BN nanoparticles compared to plain mineral oil thus offers energy savings for tribological contacts on the order of 31% and a remarkable increase in contact stability with a decreasing cycle-to-cycle standard deviation by a factor of 6.7. The nanoparticle fluid also decreases the magnitude of wear for the contact, as displayed in **Figure 3D**. The wear volume is calculated based on optical profilometry of the wear scar (*cf.* **Figure S15**) and normalized to the distance traveled by the tribometer.[51] The addition of fluorinated *h*BN nanoparticles in higher loading reduces the wear volume compared to the control oil by 71% and enters an ultralow wear regime below 1 μm^3 per mm traveled. This ultralow wear regime would enable an extended wear life for this tribological contact by nearly 3.5× as compared to standard mineral oil lubrication, enabling massive cost savings in replacement parts and downtime.

In a broad context, both *h*BN and F-*h*BN show a stabilizing and lubricating effect on the contact, but the addition of fluorine to *h*BN decreases the coefficient of friction and wear volume by a further 12% and 42%, respectively. The low friction performance of *h*BN is attributed to the weak van der Waals bonding of *h*BN sheets, which allows the sheets to shear and accommodates the tribological forces.[52] The introduction of fluorine atoms to *h*BN increases the spacing between van der Waals layers, which reduces the interaction potential and van der Waals attraction between layers of *h*BN.[21] This is highlighted by density functional theory (DFT) calculations of *h*BN and F-*h*BN (**Figure 3E-F and Figure S16**), where the fluorinated *h*BN displays an increased interlayer spacing from 3.4 Å to 4.3 Å due to intercalation (Figure 3E) which further agrees with our atomic force microscope monolayer thickness measurements (**Figure S3**). The weaker interlayer coupling results in reduced interfacial shear stress between the planes as they slide past each other, as shown in **Figure 3F**. The interlayer shear stress

decreases significantly for 10% fluorine coverage as compared to the pristine *h*BN, with only minor changes for 50% fluorine coverage. While the 50% fluorine coverage is thermodynamically stable, suggesting a high upper limit for fluorine loading, the minor difference in interfacial shear strength between 10% and 50% F loading indicates that this experimentally achieved 9.4 at.% loading achieves the majority of the theoretical friction reduction. This highlights the atomic contributions of fluorination which contribute to the reduction in contact friction and wear upon fluorination of *h*BN.

The mechanism of reduced friction and wear for the F-*h*BN dispersed lubricants was further studied by post-mortem inspection of the wear track, as seen in **Figures 3 G-H and S17**. The wear of the countersurface is shown in **Figure S18**. It can be seen that both the *h*BN and F-*h*BN form a lubricating tribofilm within the contact, which consists of compacted particles on top of the steel substrate that acts as a buffer to reduce the friction and stabilize the contact. The contact following the control mineral oil shows an interface between worn and pristine steel at the edge of the wear track but without a noticeable tribofilm. EDS analysis of the tribofilms (**Supplementary Figures S19-S21)** shows distinct boron, nitrogen, and fluorine boundaries corresponding to the respective tribofilms which confirms that the tribofilms are indeed compacted additive particles. These tribofilms typically consist of oriented van der Waals layers of 2D materials, which shear internally to provide low friction on contact and dissipate frictional forces.

Though the addition of *h*BN nanoparticles has been previously shown to decrease the friction of lubricating oils at low loading percentages, we demonstrate that F-*h*BN nanoparticles exhibit a further reduction in friction and wear by 12% and 42%, respectively, in comparison with pristine *h*BN nanoparticle lubricants. Despite being isostructural with graphene, the improved friction through fluorination of *h*BN is the opposite of graphene, which shows increased friction by a factor of more than six upon fluorination.[53,54] This is due to out-of-plane buckling of the graphene honeycomb by fluorination which disrupts the incommensurability and potential energy corrugation of the 2D sheet. For *h*BN, however, the out-of-plane deformation is very minimal,[21] which, when combined with the decreased interaction potential by fluorine intercalation, produces low interfacial shear stress and thus a highly lubricating tribofilm. The present tribological results suggest tremendous energy and cost savings by reducing the frictional energy lost in the contact and greatly extending the wear lives of the moving tribological surfaces. Furthermore, the low volume of 0.05 wt.% F-*h*BN particles in mineral oil required to achieve this lubricating regime indicates a highly economical lubricant system.

2.4. F-*h*BN as a Dielectric Material

Lastly, we also evaluate the dielectric properties of fluorinated *h*BN due to its prominence across micro and nanoelectronics in including 2D field-effect transistors and electromagnetic shielding applications. In addition to its high thermal conductivity, *h*BN offers a wide bandgap energy[55] and optimal dielectric permittivity and loss[56] making it unique amongst

nanomaterials. Optimized dielectric permittivity and loss can reduce the capacitive coupling, crosstalk, and resistance-capacitance delay effect in ultrafast microelectronic devices.[57–59] For example, *h*BN can serve as an insulating or charge tunneling layer due to its low dielectric loss and high permittivity[60,61] in 2D material field-effect transistors. The addition of fluorine, which offers a permanent dipole moment due to its electronegativity as depicted in **Figure 4A**, can further tailor the dielectric properties, making it a tunable material for microelectronics applications.

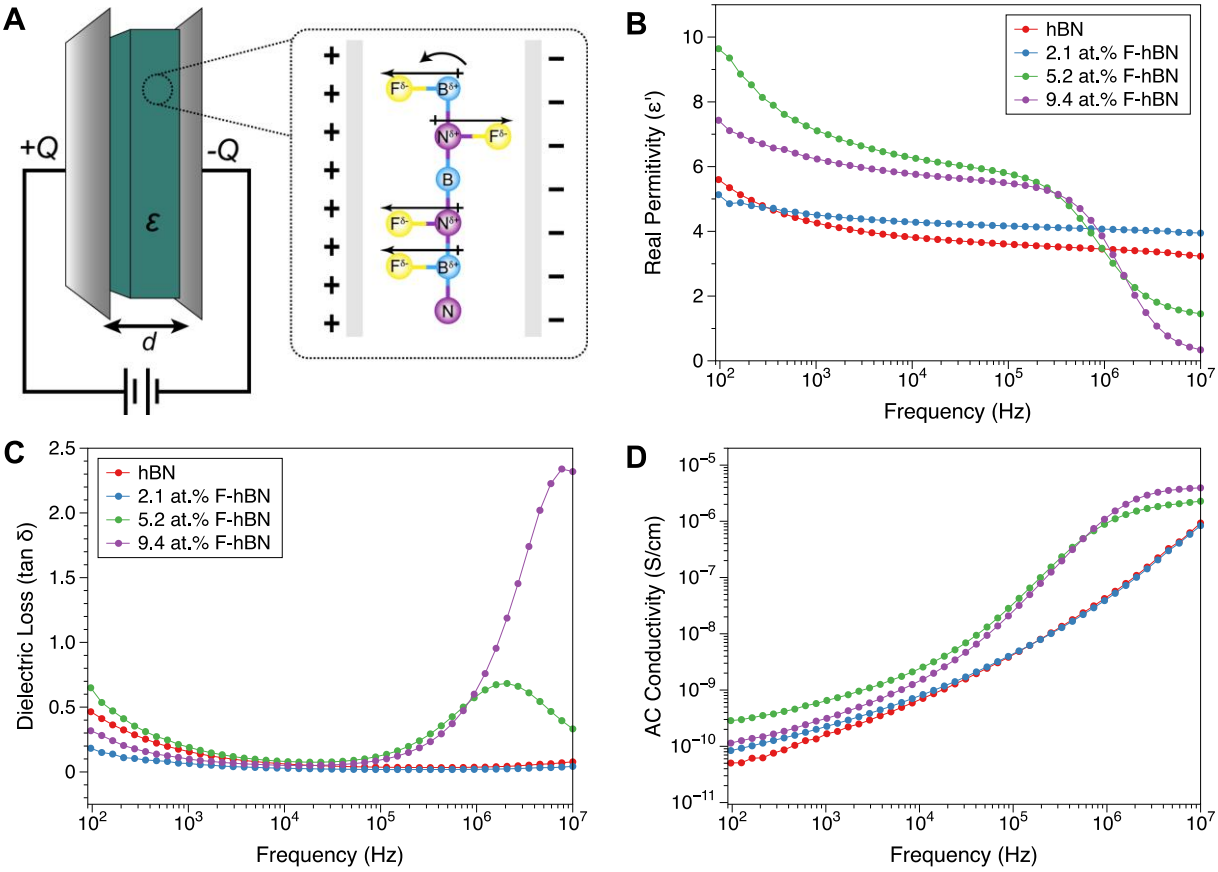

Figure 4. Dielectric permittivity and loss of F-*h*BN films. Three different F-*h*BN/CNF composite films were prepared with varying atomic percentages of fluorine. (A) Schematic depiction of parallel plate capacitor demonstrating permanent dipole moment induced by addition of fluorine to *h*BN. (B) Real permittivity studies where at low fluorine content (i.e., 2.1 at.%), the F-*h*BN/CNF films show a slight increase in the real permittivity from ε'=4.2 to 4.5 at 1 kHz compared to pristine *h*BN film. Upon increasing the fluorine content from 2.1% to 5.2 at.%, the real permittivity rises from 4.5 to 7.1 at 1 kHz. Further increase of the fluorine content to 9.4 at.% decreases the real permittivity from 7.1 to 6.3 at 1 kHz., (C) Dielectric loss measurements displaying high dependence on the fluorine content and (D) AC conductivity of F-*h*BN/nanocellulose fibers with increasing F content. Fluorination of *h*BN increased the electrical conductivity of the F-*h*BN/CNF films up to 5.2 at.%, beyond which the electrical conductivity decreased from 6.51×10^{-10} S/cm to 3.14×10^{-10} S/cm, as compared to 5.2 at.% of fluorine content.

To better understand the dielectric performance of synthesized F-*h*BN, freestanding composite films with 2 wt.% cellulose nanofibers (CNF) and F-*h*BN were derived (cf. **Figure S22**), which were then used to evaluate the broadband real permittivity and dielectric loss between a parallel plate capacitor (**Figure 4A**). Three different F-*h*BN/CNF composite films were prepared with varying atomic percentages of fluorine to clarify the sensitivity of fluorine moieties for dielectric performance. At low fluorine content (i.e., 2.1 at.%), the F-*h*BN/CNF films show a slight increase in the real permittivity from ε'=4.2 to 4.5 at 1 kHz compared to pristine *h*BN film, as seen in **Figure 4B**. Both F-*h*BN/CNF and *h*BN/CNF films exhibit a frequency-dependent behavior where their real permittivity gradually decreases with increasing frequency. Upon increasing the fluorine content from 2.1 at% to 5.2 at.%, the real permittivity rises from 4.5 to 7.1 at 1 kHz. This is directly attributed to the greater concentration of permanent dipole moments because of the incorporation of numerous negatively charged fluorine atoms on the surfaces of F-*h*BN nanosheets.[62] Further increase of the fluorine content to 9.4 at.% decreases the real permittivity from 7.1 to 6.3 at 1 kHz. The decreased permittivity can be attributed to the reduced filler size, resulting in severe edge defects. Voids can suppress the effective contact between F-*h*BN flakes, leading to decreased electrical conductivity **(Figure 4D**).

The high-frequency dielectric properties of the self-standing films also exhibit high dependence on the fluorine content. As seen in **Figure 4B**, the real permittivity of hBN and 2.1 at.% F-hBN showed a nearly flat response to the frequency, while 5.2 at.% and 9.4 at.% samples demonstrate a rapid reduction beyond 0.5 MHz. Such decay of performance is widely attributed to the domination of dipolar polarization loss.[63,64] When the frequency of the applied electric field is greater than the relaxation frequency of F-*h*BN nanosheets, the dipole mobility will be insufficient to respond to the increasing frequency.[65,66] This can lead to decreased real permittivity and increased dielectric loss at high frequency.[65,66] Correspondingly, there was a rapid increase in the loss tangent, which peaks around 2 MHz for 5.2 at.% F-hBN (**Figure 4C)**. By increasing the fluorine content from 5.2% to 9.4 at.%, the loss was intensified, and the peak appeared to shift to around 6 MHz. Such behavior is attributed to the stronger response of dipoles from increased fluorine content, which result in a shorter response time and shifts the loss peak to a higher frequency.[67] Additionally, the tangent loss peak can also occur when the applied electrical field matches with the hopping frequency. This hopping frequency increased with a higher concentration of charge carriers as fluorine content increased.[68]

Furthermore, the fluorination of *h*BN increased the electrical conductivity of the F-hBN/CNF films. As shown in **Figure 4D**, with 5.2 at.% fluorine content, the AC electrical conductivity increases by a factor of 5 from 1.66×10^{-10} S/cm to 6.51×10^{-10} S/cm at 1 kHz, as compared to the pristine *h*BN film. This increased conductivity influences the real permittivity by interfacial polarization, which indicates the inverse shapes of the curves in Figure 4 B&D.[69] In the case of 9.4 at.% of fluorine content, the electrical conductivity decreased from 6.51×10^{-10} S/cm to 3.14×10^{-10} S/cm at 1 kHz, as compared to 5.2 at.% of fluorine content.

Fluorine concentration can thus be used to tune the broadband behavior and dielectric performance of *h*BN by inducing the dipolar/interfacial polarization and polarization loss. This allows for precise tailoring of the dielectric properties of *h*BN based on the target application and operating frequency. For instance, at the 5.2 at.% fluorine content, F-*h*BN/CNF exhibits an ultralow dielectric constant of 1.46 at 10 MHz. This is extremely difficult to achieve without embracing porosity[57] which is detrimental to the mechanical and thermal properties of the material. *h*BN has been used as a low-loss dielectric material for 2D electrical components[70] which we demonstrate can be further enhanced as a low-loss material upon fluorination. As such, the fluorination of *h*BN imparts a facile and tunable technique for manufacturing thermally conductive dielectric materials for use in modern microelectronic devices.

3. Conclusion

In this work, we explored several properties of Fluorinated-*h*BN, a low-defect functionalized 2D material derived using a simple gas-phase fluorination technique. The *h*BN powders were fluorinated by passing fluorine gas at different temperatures and durations to derive fluorine functionalized *h*BN sheets without harsh treatment. The exciting physical features such as the lamellar structure of *h*BN, the weak Van der Waals forces, and the fluorine chemistries assisted in uniform dispersion of nanofillers which enabled excellent tribofilm formation and interlayer sliding making F-*h*BN an ideal lubricant to reduce friction. Additionally, the fluorine functionality in *h*BN helps in the effective dispersion of the nanofillers in lubricants and maintains centralized stability. Additionally, the dielectric performance of the F-*h*BN composite exhibited enhanced broadband real permittivity and dielectric loss due to the incorporation of numerous negatively charged fluorine atoms on the surfaces, which opens opportunity for applications in microelectronic devices. Overall, the excellent in-plane strength, the weak interlayer interactions, and surface chemical stability achieved due to the fluorination process have enabled *h*BN as an economical additive with enhanced thermal conductivity, friction and wear resistance, and dielectric properties. Collectively, these multifaceted applications which are enabled by the fluorination of *h*BN offer exceptional applicability for high thermal dissipation fluids, high-temperature lubrication, microelectronic insulation, and many other applications.

4. Materials & Methods

Synthesis of fluorinated hBN

Hexagonal boron nitride powders (Sigma Aldrich, 70nm) were dispersed in isopropyl alcohol followed by water bath sonication for 6 hours. The solution was then sonicated using a probe sonicator for 1 hour to get effective exfoliation of *h*BN powders. The solutions were then centrifuged at 2000 rpm, and the decanted solution was filtered using a Nylon filter paper with a pore size of 0.022 µm and dried overnight in vacuum oven. The dried, exfoliated *h*BN powders was fluorinated at 50ºC and 90ºC for 2 hours duration to obtain 9.4 at.% and 5.4 at.% fluorine, respectively. The fluorine content in hBN is significantly influenced by the temperature of the reaction chamber and the reaction time. 1h fluorination durations were found to present lower fluorination content at all temperatures, and the lower fluorine content observed at 90°C is due to the weak ionic N-F bond at these temperatures.[21] For the dielectric measurements, we conducted an additional fluorination at room temperature (RT) for one hour to control the fluorine content in hBN to approximately 2.1% using reduced reaction time and lower temperature.

The fluorination process was carried out by placing ~ 500 mg of exfoliated 70 nm *h*BN in a Teflon crucible and sealed tightly within a monel reactor connected to a high vacuum. The *h*BN powders inside the reactor were initially purged with a Helium (He) gas for 45 minutes to remove atmospheric oxygen from the reactor entirely. Then a mixture of He (90%) and Fluorine (10%) gas was passed into the reactor for two hours, and the temperatures were varied to 50ºC and 90ºC to derive F-hBN. The derived fluorinated hBNs were used as such without any further processing.

Caution: Fluorine is a highly reactive and toxic gas, and it is strictly advised to run the experiments in a separate fumehood with continuous airflow. Also, the gas outlet should be connected to the scrubber filled with sodium hydroxide solution to neutralize the residual gas.

Preparation of F-hBN Dispersions

To calculate the enhancement of the thermal conductivity of mineral oil (MO) due to the addition of fluorinated *h*BN, an appropriate amount of F-*h*BN was added to 20ml of MO, For example, 0.01% dispersion was obtained by adding 1.68 mg of F-*h*BN in MO. To get a homogeneous distribution and appropriate data, each type of nano-fluid was sonicated at room temperature for 2 hours, followed by magnetic stirring at 1000 rpm for 2 hours or until a clear dispersion was obtained. For solvent dispersions, bulk *h*BN and F-*h*BN in different weight percentages (0.005, 0.01 and 0.1 mg/mL) were subjected to sonication in a low-power water bath sonicator for five hours, with sporadic intervals, followed by an undisturbed period of 18 hours. The bulk particles gradually settled during this process, and the top blends of BN-solvent were selected for subsequent characterization. Visual observation and real-time photographs of the BN-solvent mixtures were captured after 30 minutes and 12 hours of preparation. However, after 24 hours, we noted significant particle aggregation and deposition in water and DCM-

based dispersions, which led us to refrain from conducting aging studies on the derived BN-solvent dispersion.

Characterization

X-ray diffraction was carried out using the Rigaku Ultima II Powder XRD system with a Cu Kα radiation (1.54 Å). The pattern was recorded for pristine and fluorinated *h*BN samples at a scan rate of 1º/min and a sampling rate of 0.02º and analyzed using PDXL software. Raman spectroscopic studies were performed using Renishaw Raman Spectrometer. Oxidation state and elemental composition were monitored using X-ray photoelectron spectroscopic performed on PHI Quantera instrument with a 5×10^{-9} Torr chamber pressure. The source power was set at 100 W, and the core-level scans' pass energies were 26 eV. Fourier transform-infra-red (FTIR) spectroscopy was used to detect the functional groups and chemical bonds in F-*h*BN. All the samples were scanned in the range of 4000–400 cm^{-1} at an average of 120 scans and with a resolution of 2 cm^{-1}. The obtained spectra were baseline corrected and normalized. FEI Titan Themis^3 S/TEM operated at 300 kV were employed to capture high-resolution images, electron diffraction spectroscopy (EDS), elemental mapping, and electron energy loss spectroscopy (EELS). Before the TEM study, the F-*h*BN samples were gently sonicated, drop-casted onto holey carbon grids, and dried in a vacuum desiccator for 24 h. Absorbance measurements of BN dispersions' were acquired using a Shimadzu 2450 UV−Visible spectrophotometer using 10 mm quartz cuvettes. The absorption was recorded from 200 to 750 nm to understand the stability of derived dispersions. Zeta Potential Analyzer was used to determine the zeta potential values of dispersed F-*h*BN particles. The measurements were acquired using Zetasizer Nano: Malvern Zen 3600 Zetasizer with the dispersions injected into the folded capillary. About 1 mL of *h*BN suspension was loaded into a measuring cell, and measurement was run at 25 °C. Each experiment was repeated three times to calculate the mean value of the experimental data.

Thermal Conductivity Measurement

Thermal conductivity of the oil samples was measured using KD-2 Pro Thermal Properties Analyzer (Decagon Devices, Inc.) using the KS-1 sensor with more than 90% of the sensor dipped inside the mineral oil or nanofluid. The thermal conductivity enhancement was calculated

$$\mathrm{TCE}\ (\%) = (\mathrm{Keff} - \mathrm{Ko}) * 100/\mathrm{Ko},$$

where K_{eff} and K_o are the thermal conductivity of nano-fluids and pristine mineral oil, respectively.

Friction and Wear Measurements

Pin on disc (POD) friction tests have been performed on an Anton Paar TRB3 tribometer; in linear reciprocating kinematics. The displacement follows a sinusoidal motion with an oscillation amplitude of +/- 3mm (6mm total amplitude), and 4Hz oscillating frequency. The test duration was fixed at 8,500 cycles which corresponds to roughly 102m of sliding distance. The sampling frequency was 400 Hz. Maximum Hertz contact pressure was chosen equal to 1.05 GPa and applied by a dead weight applying 4N load. A plate and a ball sample made of AISI52100 steel, surface roughness Ra<0.1μm, where used. A new set of samples was used for each and every friction test. The contact was immersed in 150μL lubricant volume.

Following the friction test, samples were rinsed with isopropyl alcohol and the plate further washed in isopropyl alcohol ultrasonic bath for 5min to remove all oil residue and worn particles that were not adherent to the substrate. Wear measurements were performed using Alicona Infinite Focus optical microscope which allows for 3D and roughness measurements using focus variation-based technology. The 3D data sets where then processed using Gwyddion to extract the wear volume. That volume was then normalized by the effective sliding distance undergone by the sample. Wear volume calculation is based on the approach of [ref 34]. The friction tracks morphology and compositions, on plate samples, were studied using Scanning Electron Microscopy (FEI Apreo 5 SEM) and Energy dispersive X-ray spectroscopy (EDX) (. Considering the very low thickness of the tribofilms, SEM images and EDX analysis were performed at 5keV. High magnification images have been performed at 3keV.

Dielectric Measurements

The samples' broadband alternating current (AC) conductivity and dielectric properties were carried out by a KEYSIGHT impedance analyzer (E4990A). To create freestanding films for dielectric measurements, 120 mg of hBN or F-hBN nanosheets were dispersed into 50 ml of DI water, followed by 5 mins of ultra-sonication. After that, 0.75 ml of 2wt% cellulose nanofiber solution was added to the dispersion. Then, the dispersion of the mixture was magnetically stirred for 30 mins. Finally, the self-standing films (~140 μm thickness) of hBN(F-*h*BN)/cellulose nanofibers were fabricated using a vacuum filtration system.

Statistical Analysis

Thermal dispersion analysis (Figure 2) includes N>5 for each concentration and test. Error bars represent standard error for each test, averaged across all values. No outliers were excluded.
Lubricity studies (Figure 3) include N=3 for each configuration, with friction evolution showing the mean value and shaded standard deviation per-cycle across three measurements. Wear volumes are averaged across N=3 with error bars showing standard error. No outliers were excluded.

Supporting Information

Supporting information is available from the journal or the author.

Acknowledgments

The authors acknowledge the Shared Equipment Authority (SEA) and Electron Microscopy Center (EMC), Rice University, for their support in analyzing the samples. The authors also acknowledge the Natural Sciences and Engineering Research Council and the Vanier Canada Graduate Scholarship. The authors also acknowledge Baker Hughes Company for the fluorination support.

Author Contributions

Conceptualization: A.K.M., D.S., P.S., T.F. and P.M.A.
Investigation and Analysis: D.S., A.K.M., P.S., G.C., L.M., M.H., G.G., S.Y., and V.N.K.
Supervision: V.S., R.V., C. P., C.V.S., A.K.M. and P.M.A.
Writing, Reviewing & Editing: All the authors.

Notes

The authors declare no conflict of interest.

Received: ((will be filled in by the editorial staff))
Revised: ((will be filled in by the editorial staff))
Published online: ((will be filled in by the editorial staff))

References

[1] K. Watanabe, T. Taniguchi, H. Kanda, *Nat Mater* **2004**, *3*, 404.
[2] J. C. Zheng, L. Zhang, A. v. Kretinin, S. v. Morozov, Y. B. Wang, T. Wang, X. Li, F. Ren, J. Zhang, C. Y. Lu, J. C. Chen, M. Lu, H. Q. Wang, A. K. Geim, K. S. Novoselov, *2d Mater* **2016**, *3*, DOI 10.1088/2053-1583/3/1/011004.
[3] Y. Bai, J. Zhang, Y. Wang, Z. Cao, L. An, B. Zhang, Y. Yu, J. Zhang, C. Wang, *ACS Appl Nano Mater* **2019**, DOI 10.1021/acsanm.9b00502.
[4] Ç. V. Yıldırım, M. Sarıkaya, T. Kıvak, Ş. Şirin, *Tribol Int* **2019**, *134*, 443.
[5] J. Taha-Tijerina, T. N. Narayanan, G. Gao, M. Rohde, D. A. Tsentalovich, M. Pasquali, P. M. Ajayan, *ACS Nano* **2012**, *6*, 1214.
[6] J. Taha-Tijerina, H. Ribeiro, K. Aviña, J. M. Martínez, A. P. Godoy, J. M. de O. Cremonezzi, M. A. Luciano, M. A. G. Benega, R. J. E. Andrade, G. J. M. Fechine, G. Babu, S. Castro, *Nanomaterials* **2020**, *10*, DOI 10.3390/nano10061160.
[7] M. Salehirad, M. M. A. Nikje, *Russian Journal of Applied Chemistry* **2019**, *92*, 78.
[8] I. Meric, C. R. Dean, N. Petrone, L. Wang, J. Hone, P. Kim, K. L. Shepard, *Proceedings of the IEEE* **2013**, *101*, 1609.
[9] Q. Weng, X. Wang, X. Wang, Y. Bando, D. Golberg, *Chem Soc Rev* **2016**, DOI 10.1039/c5cs00869g.
[10] G. R. Bhimanapati, D. Kozuch, J. A. Robinson, *Nanoscale* **2014**, *6*, 11671.

[11] Y. Li, T. Huang, M. Chen, L. Wu, *Chemical Engineering Journal* **2022**, *442*, DOI 10.1016/j.cej.2022.136237.
[12] I. M. Joni, R. Balgis, T. Ogi, T. Iwaki, K. Okuyama, *Colloids Surf A Physicochem Eng Asp* **2011**, *388*, 49.
[13] N. Talib, E. A. Rahim, *Tribol Int* **2018**, *118*, 89.
[14] M. K. Gupta, J. Bijwe, M. Padhan, *Lubrication Science* **2018**, *30*, 441.
[15] Q. Cai, D. Scullion, W. Gan, A. Falin, S. Zhang, K. Watanabe, T. Taniguchi, Y. Chen, E. J. G. Santos, L. H. Li, *Sci Adv* **2019**, *5*, eaav0129.
[16] I. Jo, M. T. Pettes, J. Kim, K. Watanabe, T. Taniguchi, Z. Yao, L. Shi, *Nano Lett* **2013**, *13*, 550.
[17] C. Lee, Q. Li, W. Kalb, X. Z. Liu, H. Berger, R. W. Carpick, J. Hone, *Science (1979)* **2010**, *328*, 76.
[18] C. J. Reeves, P. L. Menezes, M. R. Lovell, T. C. Jen, *Tribol Lett* **2013**, *51*, 437.
[19] A. S. Nazarov, V. N. Demin, E. D. Grayfer, A. I. Bulavchenko, A. T. Arymbaeva, H. J. Shin, J. Y. Choi, V. E. Fedorov, *Chem Asian J* **2012**, *7*, 554.
[20] J. Ren, L. Stagi, P. Innocenzi, *J Mater Sci* **2021**, *56*, 4053.
[21] A. K. Meiyazhagan, P. Serles, D. Salpekar, E. F. Oliveira, L. B. Alemany, R. Fu, G. Gao, T. Arif, R. Vajtai, V. Swaminathan, D. S. Galvao, V. N. Khabashesku, T. Filleter, P. M. Ajayan, *Advanced Materials* **2021**, 2106084.
[22] S. Roy, X. Zhang, A. B. Puthirath, A. Meiyazhagan, S. Bhattacharyya, M. M. Rahman, G. Babu, S. Susarla, S. K. Saju, M. K. Tran, L. M. Sassi, M. A. S. R. Saadi, J. Lai, O. Sahin, S. M. Sajadi, B. Dharmarajan, D. Salpekar, N. Chakingal, A. Baburaj, X. Shuai, A. Adumbumkulath, K. A. Miller, J. M. Gayle, A. Ajnsztajn, T. Prasankumar, V. V. J. Harikrishnan, V. Ojha, H. Kannan, A. Z. Khater, Z. Zhu, S. A. Iyengar, P. A. da S. Autreto, E. F. Oliveira, G. Gao, A. G. Birdwell, M. R. Neupane, T. G. Ivanov, J. Taha-Tijerina, R. M. Yadav, S. Arepalli, R. Vajtai, P. M. Ajayan, *Advanced Materials* **2021**, *33*, DOI 10.1002/adma.202101589.
[23] F. Xiao, S. Naficy, G. Casillas, M. H. Khan, T. Katkus, L. Jiang, H. Liu, H. Li, Z. Huang, *Advanced Materials* **2015**, *27*, 7196.
[24] H. Wu, S. Yin, Y. Du, L. Wang, Y. Yang, H. Wang, *ACS Appl Nano Mater* **2020**, *3*, 9108.
[25] W. Wang, M. Zhao, D. Jiang, X. Zhou, J. He, *Ceram Int* **2022**, *48*, 2763.
[26] B. Karuppaiah, J. Anupriya, S. M. Chen, S. J. Park, *Process Safety and Environmental Protection* **2023**, *176*, 292.
[27] L. Song, Z. Liu, A. L. M. Reddy, N. T. Narayanan, J. Taha-Tijerina, J. Peng, G. Gao, J. Lou, R. Vajtai, P. M. Ajayan, *Advanced Materials* **2012**, *24*, 4878.
[28] A. D. Smith McWilliams, C. Martínez-Jiménez, A. Matatyaho Ya'Akobi, C. J. Ginestra, Y. Talmon, M. Pasquali, A. A. Martí, *ACS Appl Nano Mater* **2021**, *4*, 142.
[29] Q. Weng, X. Wang, X. Wang, Y. Bando, D. Golberg, *Chem Soc Rev* **2016**, *45*, 3989.
[30] M. Li, G. Huang, X. Chen, J. Yin, P. Zhang, Y. Yao, J. Shen, Y. Wu, J. Huang, *Nano Today* **2022**, *44*, DOI 10.1016/j.nantod.2022.101486.
[31] M. Du, X. Li, A. Wang, Y. Wu, X. Hao, M. Zhao, *Angewandte Chemie - International Edition* **2014**, DOI 10.1002/anie.201308294.
[32] S. Radhakrishnan, D. Das, A. Samanta, C. A. De Los Reyes, L. Deng, L. B. Alemany, T. K. Weldeghiorghis, V. N. Khabashesku, V. Kochat, Z. Jin, P. M. Sudeep, A. A. Martí, C. W. Chu, A. Roy, C. S. Tiwary, A. K. Singh, P. M. Ajayan, *Sci Adv* **2017**, DOI 10.1126/sciadv.1700842.
[33] S. Hong, C. S. Lee, M. H. Lee, Y. Lee, K. Y. Ma, G. Kim, S. I. Yoon, K. Ihm, K. J. Kim, T. J. Shin, S. W. Kim, E. chae Jeon, H. Jeon, J. Y. Kim, H. I. Lee, Z. Lee, A. Antidormi, S. Roche, M. Chhowalla, H. J. Shin, H. S. Shin, *Nature* **2020**, *582*, 511.
[34] X. Wu, Q. Han, *Comput Mater Sci* **2020**, *184*, DOI 10.1016/j.commatsci.2020.109938.

[35] H. Jin, Y. Li, X. Li, Z. Shi, H. Xia, Z. Xu, G. Qiao, *Mater Lett* **2016**, *175*, 244.
[36] J. Zhou, Z. Lin, H. Ren, X. Duan, I. Shakir, Y. Huang, X. Duan, *Advanced Materials* **2021**, *33*, DOI 10.1002/adma.202004557.
[37] K. Leng, Z. Chen, X. Zhao, W. Tang, B. Tian, C. T. Nai, W. Zhou, K. P. Loh, *ACS Nano* **2016**, *10*, 9208.
[38] Z. Dong, H. Xu, F. Liang, C. Luo, C. Wang, Z. Y. Cao, X. J. Chen, J. Zhang, X. Wu, *Molecules* **2019**, *24*, DOI 10.3390/molecules24010088.
[39] Y. Li, N. Lv, C. Wang, J. Zhang, W. Fu, J. Yin, H. Li, W. Zhu, H. Li, *J Mol Graph Model* **2020**, *101*, DOI 10.1016/j.jmgm.2020.107715.
[40] A. ul Ahmad, H. Liang, Q. Abbas, S. Ali, M. Iqbal, A. Farid, A. Abbas, Z. Farooq, *Ceram Int* **2019**, DOI 10.1016/j.ceramint.2019.06.164.
[41] S. Nadeem, A. Shah, S. Shahabuddin, M. Faizul, M. Sabri, K. L. Malaysia, *International Journal of Advanced Science and Technology* **2020**, *29*, 304.
[42] C. Srinivasan, R. Saraswathi, *Curr Sci* **2012**, *102*.
[43] M. M. Bhunia, K. Panigrahi, S. Das, K. K. Chattopadhyay, P. Chattopadhyay, *Carbon N Y* **2018**, *139*, 1010.
[44] D. Lee, J. W. Kim, B. G. Kim, *Journal of Physical Chemistry B* **2006**, *110*, 4323.
[45] J. Taha-Tijerina, T. N. Narayanan, G. Gao, M. Rohde, D. A. Tsentalovich, M. Pasquali, P. M. Ajayan, *ACS Nano* **2012**, *6*, 1214.
[46] D. Demille, R. V Krems, J. Ye, I. Lesanovsky, P. Zoller, K. K. Lehmann, J. K. G. Watson, S. C. Wofsy, E. L. Hamilton, H. Crowell, C. Vadla, K. Niemax, S. T. Rittenhouse, D. Booth, H. R. Sadeghpour, J. P. Shaffer, S. A. Miller, G. Raithel, F. Merkt, J. Deiglmayr, A. S. Dickinson, H. R. Sadeghpour, P. R. Hemmer, U. Thumm, I. I. Fabrikant, C. H. Greene, H. R. Sadeghpour, I. I. Ryabtsev, D. B. Tretyakov, V. M. Entin, *Science (1979)* **2015**, *348*, 102.
[47] J. Zhao, J. Mao, Y. Li, Y. He, J. Luo, *Appl Surf Sci* **2018**, *434*, 21.
[48] J. C. Spear, B. W. Ewers, J. D. Batteas, *Nano Today* **2015**, *10*, 301.
[49] X. Zhang, H. Xu, J. Wang, X. Ye, W. Lei, M. Xue, H. Tang, C. Li, *Nanoscale Res Lett* **2016**, *11*, DOI 10.1186/s11671-016-1659-3.
[50] O. N. Çelik, N. Ay, Y. Göncü, *Particulate Science and Technology* **2013**, *31*, 501.
[51] P. H. Cornuault, G. Colas, A. Lenain, R. Daudin, S. Gravier, *Tribol Int* **2020**, *141*, DOI 10.1016/j.triboint.2019.105957.
[52] J. P. Oviedo, S. Kc, N. Lu, J. Wang, K. Cho, R. M. Wallace, M. J. Kim, *ACS Nano* **2015**, *9*, 1543.
[53] S. Kwon, J. H. Ko, K. J. Jeon, Y. H. Kim, J. Y. Park, *Nano Lett* **2012**, *12*, 6043.
[54] Q. Li, X. Z. Liu, S. P. Kim, V. B. Shenoy, P. E. Sheehan, J. T. Robinson, R. W. Carpick, *Nano Lett* **2014**, *14*, 5212.
[55] K. Watanabe, T. Taniguchi, H. Kanda, *Nat Mater* **2004**, *3*, 404.
[56] A. Laturia, M. L. Van de Put, W. G. Vandenberghe, *NPJ 2D Mater Appl* **2018**, *2*, 6.
[57] R. D. Miller, *Science (1979)* **1999**, *286*, 421.
[58] Y. Xue, X. Zhou, T. Zhan, B. Jiang, Q. Guo, X. Fu, K. Shimamura, Y. Xu, T. Mori, P. Dai, Y. Bando, C. Tang, D. Golberg, *Adv Funct Mater* **2018**, *28*, 1801205.
[59] M. Hamidinejad, A. Zandieh, J. H. J. H. Lee, J. Papillon, B. Zhao, N. Moghimian, E. Maire, T. Filleter, C. C. B. Park, *ACS Appl Mater Interfaces* **2019**, *11*, 41726.
[60] I. Meric, C. Dean, A. Young, J. Hone, P. Kim, K. L. Shepard, *Technical Digest - International Electron Devices Meeting, IEDM* **2010**, DOI 10.1109/IEDM.2010.5703419.
[61] M. Sup Choi, G. H. Lee, Y. J. Yu, D. Y. Lee, S. Hwan Lee, P. Kim, J. Hone, W. J. Yoo, *Nat Commun* **2013**, *4*, 1.
[62] P. Martins, A. C. Lopes, S. Lanceros-Mendez, *Prog Polym Sci* **2014**, *39*, 683.
[63] Y. Jin, N. Xia, R. A. Gerhardt, *Nano Energy* **2016**, *30*, 407.

[64] H. Tang, Z. Zhou, C. C. Bowland, H. A. Sodano, *Nano Energy* **2015**, *17*, 302.
[65] A. K. Jonscher, *Dielectric Relaxation in Solids*, **1999**.
[66] G. W. Bak, A. K. Jonscher, *J Mater Sci* **1999**, *34*, 5505.
[67] C. Wu, Z. Li, G. M. Treich, *Appl. Phys. Lett* **2019**, *115*, 163901.
[68] J. Chand, M. Singh, *J Alloys Compd* **2009**, *486*, 376.
[69] C.-W. Nan, Y. Shen, J. Ma, *Annu Rev Mater Res* **2010**, *40*, 131.
[70] J. I. J. Wang, M. A. Yamoah, Q. Li, A. H. Karamlou, T. Dinh, B. Kannan, J. Braumüller, D. Kim, A. J. Melville, S. E. Muschinske, B. M. Niedzielski, K. Serniak, Y. Sung, R. Winik, J. L. Yoder, M. E. Schwartz, K. Watanabe, T. Taniguchi, T. P. Orlando, S. Gustavsson, P. Jarillo-Herrero, W. D. Oliver, *Nat Mater* **2022**, *21*, 398.

Table of Contents:

Fluorination of Hexagonal Boron Nitride unlocks multifunctional applications with high performance lubrication of steel contacts, enhanced thermal conductivity for oil dispersions, and tunable dielectric permittivity with frequency variation. These collective engineering applications are each improved by adding 10% fluorine to hBN nanoparticles.

Graphic Table of Contents: